Editors' Suggestion

Noncapillary Wave Dynamics due to Interfacial Coupling with Plasma Patterns at a Liquid Surface

Oles Dubrovski,[1,§] Jinyu Yang,[1,§] Felipe Veloso,[2] David B. Go,[1,3,*] Hsueh-Chia Chang,[1,3,†] and Paul Rumbach[1,‡]
[1]Department of Aerospace and Mechanical Engineering, University of Notre Dame, Notre Dame, Indiana 46556, USA
[2]Instituto de Física, Pontificia Universidad Catolica de Chile, Santiago, Region Metropolitana, Chile
[3]Department of Chemical and Biomolecular Engineering, University of Notre Dame, Notre Dame, Indiana 46556, USA

(Received 24 October 2023; revised 31 May 2024; accepted 25 July 2024; published 5 September 2024)

We identify a new class of surface waves that arise at a plasma-liquid interface due to resonant coupling between discrete plasma pattern modes and a continuum of interfacial liquid surface wave modes. A wave mode is selected due to localized excitation by the plasma, and standing waves result when waves excited from different locations interact. These waves propagate with a slower phase velocity than traditional capillary waves, but exhibit the same damping behavior with respect to liquid viscosity. Surface tension does not appear to play a significant role. We propose a curvature-dependent Maxwell pressure mechanism to explain these nondispersive interfacial waves in the presence of plasma.

DOI: 10.1103/PhysRevLett.133.105301

Plasma interactions with liquids can promote unique physiochemical interactions dictated by delivery of reactive plasma species, including electrons, ions, and radicals, across the gas-liquid interface [1]. These reactions are typically limited by the transport of reactants in the liquid phase. For example, plasma systems used to destroy per- and polyfluoroalkyl substances (PFAS) in wastewater are limited by transport of PFAS to the interface [2], because the dominant reactive plasma species (solvated electrons and hydroxyl radicals) do not penetrate far into the liquid [3]. Direct current (dc) plasma discharges are known to self-organize into patterned states and form coherent structures under the right conditions, including forming intricate patterns on resistive anode surfaces, such as doped silicon [4,5] or liquid saline solutions [6–9]. In medical applications, patterns have been shown to introduce favorable conditions in terms of current density and heat generation for the treatment of cancer cells [10]. Self-organization in natural systems often arise because of transport optimization [11,12]. Inherent coupling of plasma self-organization with solution advective transport could naturally lead to highly efficient reaction promotion at a plasma gas-liquid interface.

The complex interactions between plasma and liquids involve physics at highly disparate time and length scales, making their dynamics difficult to analyze even with full numerical simulations [13,14]. Rumbach *et al.* [15] accurately predicted the transition from a uniform spot to an annular ring plasma pattern by applying a Turing-like theory [11] for radial transport-reaction pattern formation. The Turing mechanism establishes quasiequilibrium static patterns with millimeter length scales that are governed by the net electron axial flux into the liquid. This flux is gated by both liquid and plasma ion charge distributions in the nanometer and micron-scale Debye layers on both the liquid and plasma side of the interface, respectively [16].

At higher currents, liquid anode dc plasma patterns exhibit dynamic fluctuations, which currently are not predicted by any existing theory. The ring pattern loses its stability and dynamically oscillates between a continuous annulus ring and four individual plasma spots at a frequency of around 10^2 Hz, similar to an $m = 4$ standing wave mode on a drumhead, as shown in Figs. 1(e) and 2(a). Increasing the current further introduces more complex shapes and pattern dynamics, such as rotating spotted rings and spokes [6], that often depend on the electrolyte salt [9,17]. Dynamic plasma patterns in these systems have been reported with characteristic frequencies near 100–1000 Hz [7,17,18], which is much slower than plasma timescales that produce fluctuations at 10^5–10^6 Hz [19].

Low frequency plasma pattern oscillations suggest that the motion is limited or controlled by electrohydrodynamic (EHD) coupling to the water, likely in the form of interfacial liquid surface waves. Specifically, the reaction-diffusion wave number of the plasma pattern selects a specific wave mode from the continuum of liquid surface waves. In this Letter, we present experimental evidence for this in the form of measured dispersion relations. Changing the solution ionic strength effectively changes the reaction-diffusion wave number for plasma electrons by altering the interfacial electrostatic conditions. Increasing the solution viscosity decreases the measured wave frequency in a

*Contact author: dgo@nd.edu
†Contact author: hchang@nd.edu
‡Contact author: prumbach@nd.edu
§These authors contributed equally to this work.

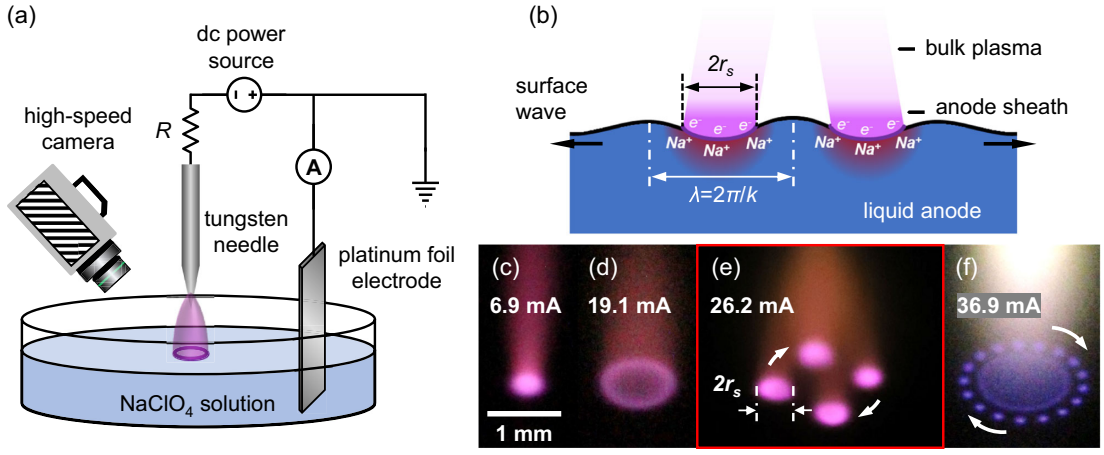

FIG. 1. (a) Schematic of liquid anode glow discharge system. The discharge is generated by applying dc voltage through a ballast resistor R to a needle cathode suspended above a liquid surface with a submerged, grounded counterelectrode. (b) Illustration of the electrostatics of the plasma-liquid interface. The space charge field in the plasma's anode sheath induces waves on the liquid surface, whose wavelength is determined by the reaction and diffusion of electrons in the anode sheath. (c)–(f) Show patterns for a 128 mM $NaClO_4$ solution. As the current increases in the system, the plasma progresses from a uniform spot (c) to a continuous annular ring (d). At higher currents, the annular ring breaks into four spots (e) and oscillates between the two conditions. At still greater currents, a more complex pattern (f) is observed.

manner mathematically consistent with well-established models for the viscous damping of liquid surface waves [20].

Interestingly, the measured frequencies are an order of magnitude lower than predicted by capillary wave theory. Plasma pattern wavelengths are < 1 mm, which yields frequencies of 10^3–10^4 Hz using the well-known inviscid capillary wave formula $\omega_0 = (\gamma k^3/\rho)^{1/2}$, where γ is surface tension and ρ is liquid density. Unlike capillary waves, the waves also appear to be nondispersive with a wave-number-independent phase velocity. We hypothesize that electrostatic stresses at the plasma-liquid interface negate the effects of surface tension, and we derive a new theoretical inviscid dispersion relation based entirely on curvature-dependent Maxwell pressure that underscores the electrostatic coupling between the plasma and liquid phase.

Figure 1(a) illustrates our experimental apparatus. A tungsten needle electrode (3.175 mm diameter) is suspended 4 mm above the surface of the electrolyte solution, consisting of dissolved sodium perchlorate ($NaClO_4$) in concentrations ranging from $I_S = 16$ to 256 mM. Glycerol was added from 0% to 20% to vary the viscosity of the solution from $\nu = 1.0 \times 10^{-6}$ to 1.9×10^{-6} m^2 s^{-1} [21]. A grounded platinum (Pt) foil submerged beneath the liquid surface serves as the counterelectrode. A discharge is formed by applying roughly -2 kV to the tungsten electrode across a ballast resistor of 47 kΩ using a high voltage dc power supply (Power Designs INC., Model 1570). Current was monitored using a digital multimeter (Amprobe, AM-510) connected to the Pt foil counter-electrode. Pattern oscillations were filmed with a high-speed camera (Photron FASTCAM, SA4) angled 45° to the liquid surface at a rate of 10^4 fps, and the oscillation frequency was extracted from each video. Static photographs were taken using a Canon EOS 6D Mark II camera with an exposure of 1 ms and have been contrast enhanced for clarity. All experiments were conducted in atmospheric air and repeated at least $n = 9$ times to ensure repeatability. Uncertainty for each measured mean frequency was estimated using the random error of the 9 measurements with a Student's t value of 2.306 (95% confidence level).

Our experiments show that for the ionic strength range of 16 to 256 mM, the transition from a uniform spot to an annulus ring pattern occurs at approximately 10 mA [Figs. 1(c) and 1(d)], consistent with prior work [15]. Around 25 mA, the ring pattern enters into an unstable regime, where it oscillates between the annulus ring pattern and a four-spot pattern [Fig. 1(e); see Sec. S1 in Supplemental Material [22] for still frames and a video]. At approximately 30.0 mA, it transitions into a quasistable, complex spotted pattern [Fig. 1(f)]. The oscillation frequency depends on both the ionic strength and viscosity of the solution as shown in Fig. 2, exhibiting a stronger viscosity dependence at low conductivities. The frequency is on the order of 10^2 Hz, which is considerably slower than any plasma chemical reactions [23], but it is within the scope of fluid motion frequencies, specifically surface waves [24–27]. As Fig. 2(a) shows, the measured wave frequency decreases with solution viscosity, just as expected for liquid surface waves.

There is a sensitive but distinct dependence of the oscillation frequency with respect to both viscosity and ionic strength. As shown by Rumbach *et al.* [15], the length scale of the patterns generated from a plasma spot is

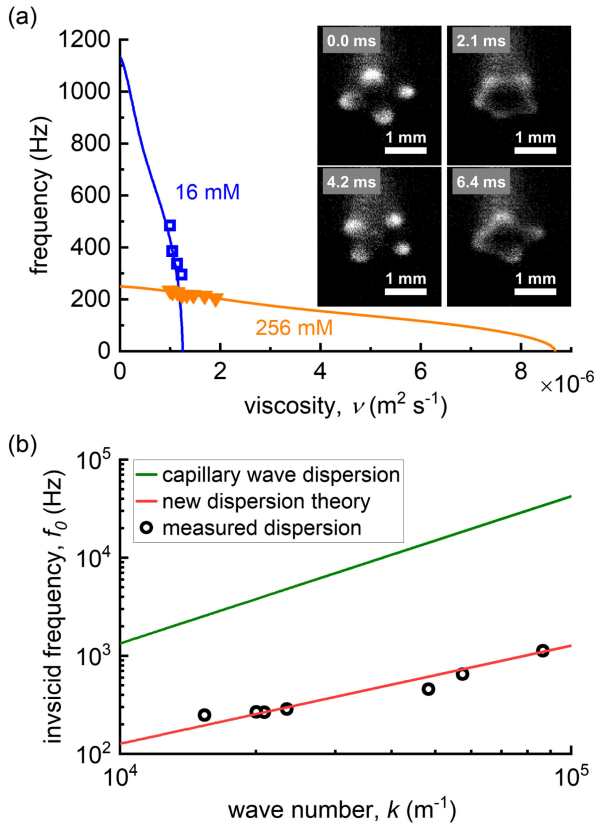

FIG. 2. (a) Pattern oscillation frequencies measured using high-speed imaging (inset) for various solution viscosities and ionic strengths. (b) The inviscid frequency f_0 for $\nu = 0$ and wave number k were extrapolated using Eq. (4) for various values of ionic strength. Extrapolated inviscid frequencies are compared to the traditional capillary wave dispersion and Eq. (5).

determined by a balance between the electron-avalanche autocatalytic reaction and electron diffusion. In a strong electric field, electron impact ionization is the dominant reaction, and other reactions, such as electron attachment, can be neglected. The relevant wave number k for the plasma pattern and subsequent capillary waves is

$$k = \sqrt{\frac{\alpha \mu_e E_r}{D_e}}, \tag{1}$$

where $\alpha = Ap\exp(-Bp/E_r)$ is the Townsend electron impact ionization coefficient for the avalanche autocatalytic reaction, μ_e is the electron mobility, E_r is the radial electric field that accelerates the electrons for the avalanche autocatalytic reaction, and $D_e = 0.415\ \mathrm{m}^2/\mathrm{s}$ is the electron diffusivity in the plasma [15]. The pressure is assumed to be $p = 750$ torr, and other parameters, including the ionization parameters A and B, are approximated for humid air using the BOLSIG+ Boltzmann solver [28]. Further discussion and a table of values can be found in Supplemental Material [22].

The average radial electric field depends on the plasma electron density n_0 and plasma spot radius r_s, such that $E_r = (qn_0/4\epsilon_0)r_s$, where q is the elementary charge and ϵ_0 is the permittivity of free space [15]. Hence, the wave number of the excited patterns is a function of the plasma spot radius r_s, which depends on both the plasma current I, experimentally controlled to be 26.2 mA, and the current density j. The current density j is determined by the conductivity and field of both the plasma and liquid [16]. Matching the flux in the plasma sheath and solution Debye layer, we have an explicit formula for j as a function of liquid ionic strength I_s [16],

$$j(I_s) = j_\infty \frac{1 - \exp(-bI_s)}{\mathrm{erf}\left(\sqrt{bI_s}\right)}, \tag{2}$$

where $j_\infty = D_e\sqrt{2q^3 n_0^3/(\pi\epsilon_0 V_{Te})}$ is the maximum current density allowed by the plasma and $b = 80qV_L^2/(n_0 V_{Te} k_b T_L)$ [16]. The electron thermal voltage is assumed to be $V_{Te} = 1$ V, and the liquid temperature to be $T_L = 320$ K. The plasma electron density $n_0 = 2.35 \times 10^{18}\ \mathrm{m}^{-3}$ and voltage drop across the liquid Debye layer $V_L = 8.6\ \mu\mathrm{V}$ are determined experimentally by fitting Eq. (2) to measured current density versus ionic strength data [16]. The current density increases with increasing ionic strength, eventually reaching a constant limit j_∞, where it is no longer limited by solution conductivity, but by the plasma conductivity instead. The plasma spot radius is

$$r_s = \sqrt{\frac{I}{m\pi j}}, \tag{3}$$

where m is the number of spots. Thus, the plasma current I and solution ionic strength I_s can be used to control the radial electric field E_r and plasma wave number k. The plasma radius decreases toward a constant asymptote at high ionic strength due to the limiting current density phenomenon related to j_∞, which also causes the plasma radius r_s, radial field E_r, and the plasma wave number k to asymptote. This high ionic-strength asymptote is observed in the wave number of Fig. 3(a).

Figure 3(a) shows both the experimental and theoretical wave number and inviscid frequency as a function of the solution ionic strength. To compute the theoretical curves, phase velocities c were acquired experimentally using high-speed imaging by placing the camera aligned with the liquid surface, as shown in Fig. 3(b) and discussed in Sec. S4 of Supplemental Material [22]. The experimental inviscid frequency $\omega_{0,\mathrm{exp}}$ and wave number k_{exp} are extrapolated by curve fitting the experimental data, such as those in Figs. 2 and S2 of Supplemental Material [22], with the viscous capillary wave dispersion relation [29] (gravity is negligible for these waves)

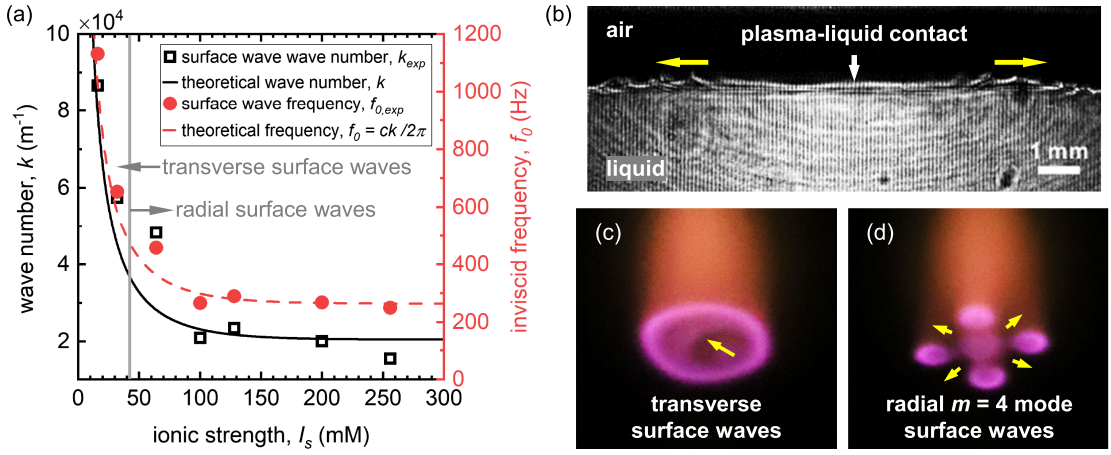

FIG. 3. (a) Extrapolated wave numbers k (black open squares) and inviscid frequencies f_0 (red solid circles) as a function of ionic strength. Curves depict theory based on Eq. (1) for k and $f_0 = ck/2\pi$, where the empirical values for j_∞ and b in Eq. (3) were used from [15]. Plasma parameters of $n_0 = 2.35 \times 10^{18}$ m^{-3} and $I = 26.2$ mA were used for the theoretical lines. (b) Side-view still frame of the plasma impinging on the liquid surface, inducing surface waves propagating radially outward at a measurable phase velocity c. Photographs of (c) a deformed ring with induced transverse waves at 32 mM and (d) the four spots with radial waves at 48 mM. The yellow arrows indicate the propagation direction of the waves.

$$(2\nu k^2 - i\omega)^2 + \omega_0^2 = 4\nu^2 k^4 \sqrt{1 - \frac{i\omega}{\nu k^2}}, \tag{4}$$

where ν is the kinematic viscosity of the solution, k is the wave number, $\mathrm{Re}[\omega]$ is the temporal frequency, $\mathrm{Im}[\omega]$ is the viscous damping rate, and ω_0 is the natural resonance frequency or inviscid frequency of the particular wave number k.

The damping of the observed frequencies ω scale with wave number k and viscosity ν as predicted by Eq. (4). However, the data are not consistent with the well-known inviscid capillary wave formula $\omega_0 = (\gamma k^3/\rho)^{1/2}$, which predicts frequencies an order of magnitude greater. Shown in Fig. 2(b), the experimental data follow the nondispersive relation $\omega_0 = ck$ with a constant phase velocity $c \approx 0.08$ ms^{-1}. Others have shown that a uniform electrostatic field typically reduces liquid surface wave frequency and phase velocity [30,31]. Plasma-liquid surface waves represent an extreme example of this, with a nonuniform electric field and considerable current density across the interface. This likely creates an interfacial Helmholtz double layer that may alter the physiochemical structure of the water and reduce the surface tension [32–34].

We believe these waves constitute a new class of liquid surface waves, whose behavior is unaffected by surface tension and dictated entirely by EHD interactions. In the Appendix, we derive a new dispersion relation based on the perturbation of electrostatic stresses due to surface curvature in a plasma medium [35]. We hypothesize that the effects of surface tension are neutralized by the intense electric field across the plasma liquid interface, and we propose a new inviscid dispersion relation

$$\omega_0 = \left(\frac{qn_0 L_p E_0}{\rho}\right)^{1/2} k, \tag{5}$$

where E_0 is the uniform normal component of the electric field, and $L_p = \sqrt{\epsilon_0 V_T/qn_0}$ is the plasma Debye length. Using the values for n_0 and V_T listed earlier and $E_0 = 3.5 \times 10^6$ Vm^{-1} yields a theoretical phase velocity $c = 0.08$ ms^{-1}, which matches our experimental data. The classic inviscid capillary wave dispersion and the new plasma-liquid wave dispersion relations are compared with the experimental data in Fig. 2(b).

Interestingly, at low ionic strengths (16 and 32 mM), we observed a dramatically different dynamic behavior. Rather than the four spots shown in Fig. 1(e), we observed a deforming annulus ring with visible transverse surface waves (Cartesian plane waves) inside with significantly shorter wavelengths [Figs. 3(a) and 3(c)] as we move away from the limiting current region. In this low-conductivity limit below the limiting current, the high wave number k reduces the viscous wave decay length $L_D = \mathrm{Re}[\omega]/\mathrm{Im}[\omega]k$, such that $L_D \ll r_s$. (Fig. S5 in Supplemental Material [22] plots these two length scales, showing their divergence at low ionic strength.) Thus, surface waves emanating from nascent plasma spots are damped before they can interact and form standing waves, and we observe transverse plane waves propagating inward from the edges of the plasma ring.

The dispersion relation given by Eq. (4) can be nondimensionalized by defining a nondimensional frequency $\omega^* = \omega/\omega_0$ and a viscous damping ratio $\zeta = 2\nu k^2/\omega_0$ to obtain

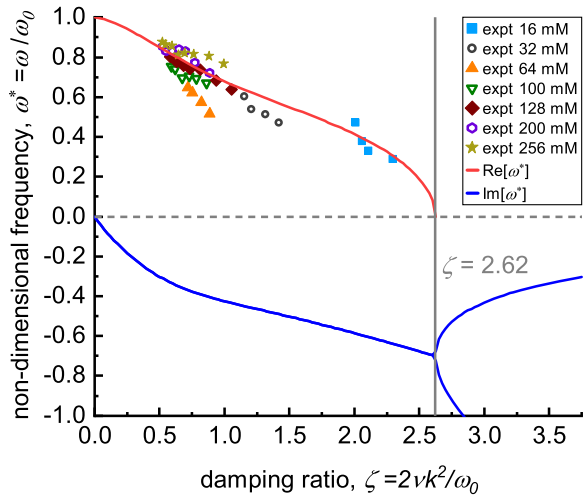

FIG. 4. The physical roots of Eq. (6) as a function of ζ consist of a frequency component, $\mathrm{Re}[\omega^*]$ plotted in red, and a damping rate, $\mathrm{Im}[\omega^*]$ plotted in blue. Nondimensionalized frequency data, for various values of solution viscosity and ionic strength, collapse onto the real part of the root of Eq. (6).

$$(\zeta - i\omega^*)^2 + 1 = \zeta^2\sqrt{1 - i\frac{2\omega^*}{\zeta}}. \tag{6}$$

Note that the viscous damping ratio is essentially the inverse Reynolds number ($\zeta = \mathrm{Re}^{-1}$) for a viscous capillary wave, where $\mathrm{Re} \equiv (\omega_0/k \times 1/k)/2\nu$ [36,37]. It is small at low wave numbers and low viscosity, but can reach large values $>> 1$ as the wave number k blows up at low ionic strengths [Fig. 3(a)] or high viscosity. Equation (6) can be written as a quartic polynomial with four roots for ω^*, plotted in Fig. S6 in Supplemental Material [22]. Two of the most stable modes are considered nonphysical and are typically ignored. The physical pair of roots, shown in Fig. 4, have a real part corresponding to temporal frequency and an imaginary part corresponding to damping rate. At a critical value of $\zeta \approx 2.62$, the real part vanishes and the waves become overdamped.

Also shown in Fig. 4 are the experimental data, which have been similarly nondimensionalized, where ζ is computed from the experimental viscosity value ν and theoretical plasma pattern wave number k computed using Eq. (1) for each ionic strength, and ω^* is computed by dividing every measured frequency by $\omega_0 = ck$, using the phase velocity $c = 0.08\ \mathrm{ms}^{-1}$. The nondimensional experimental data points collapse onto the theoretical line, which corresponds to the solution of Eq. (6). Importantly, no pattern oscillations were observed beyond the critical value $\zeta = 2.62$, where high viscosity prevents wave motion. The collapse of the data using both the theoretical wave number for plasma patterns combined with the theoretical dispersion relation Eq. (6) shows that the size of the patterns is dictated by plasma processes, while the transient behavior is limited by the advection of solvated salt cations (Na^+) via viscous surface waves.

We have hence verified that the dynamics of self-organized plasma patterns on a liquid anode surface are driven by a unique class of EHD surface waves. Liquid transport is likely also a limiting factor in higher order pattern oscillations, such as the rotation of radially symmetric patterns of spots or spokes [6]. While there are inherent plasma processes, including ionization [15] and electron attachment to electronegative molecules [6,38], that affect pattern formation, this work shows that the solution plays a critical role in both the form and behavior of such self-organization. We have proposed a simple model involving the surface curvature, yielding a nondispersive wave speed that quantitatively matches our data. However, there are many other EHD effects that should be considered, such as electrostatic shear stress and the electromigration of solution ions, which likely effect plasma-liquid surface waves and play an important role in various plasma applications [39,40]. Understanding the nonlinear EHD coupling between plasma and viscous liquids will require more sophisticated theoretical techniques and numerical simulations.

Acknowledgments—O. D. and D. B. G. acknowledge financial support from the National Science Foundation through Grant No. PHY-2206420 and from the Army Research Office through Award No. W911NF-23-1–0010. F. V. and D. B. G. also acknowledge support from Notre Dame—Universidad Católica|Chile Scholars Joint Research Award.

[1] P. J. Bruggeman *et al.*, Plasma–liquid interactions: A review and roadmap, Plasma Sources Sci. Technol. **25**, 053002 (2016).
[2] R. K. Singh, E. Brown, S. Mededovic Thagard, and T. M. Holsen, Treatment of PFAS-containing landfill leachate using an enhanced contact plasma reactor, J. Hazard. Mater. **408**, 124452 (2021).
[3] P. Rumbach, D. M. Bartels, and D. B. Go, The penetration and concentration of solvated electrons and hydroxyl radicals at a plasma-liquid interface, Plasma Sources Sci. Technol. **27**, 115013 (2018).
[4] Yu. A. Astrov and Yu. A. Logvin, Formation of clusters of localized states in a gas discharge system via a self-completion scenario, Phys. Rev. Lett. **79**, 2983 (1997).
[5] Yu. A. Astrov, I. Müller, E. Ammelt, and H.-G. Purwins, Zigzag destabilized spirals and targets, Phys. Rev. Lett. **80**, 5341 (1998).
[6] N. Shirai, S. Uchida, and F. Tochikubo, Influence of oxygen gas on characteristics of self-organized luminous pattern formation observed in an atmospheric dc glow discharge using a liquid electrode, Plasma Sources Sci. Technol. **23**, 054010 (2014).
[7] T. Verreycken, P. Bruggeman, and C. Leys, Anode pattern formation in atmospheric pressure air glow discharges with water anode, J. Appl. Phys. **105**, 083312 (2009).

[8] Y. E. Kovach, M. C. García, and J. E. Foster, Optical emission spectroscopy investigation of a 1-atm DC glow discharge with liquid anode and associated self-organization patterns, IEEE Trans. Plasma Sci. **47**, 3214 (2019).

[9] J. E. Foster, Y. E. Kovach, J. Lai, and M. C. Garcia, Self-organization in 1 atm DC glows with liquid anodes: current understanding and potential applications, Plasma Sources Sci. Technol. **29**, 034004 (2020).

[10] Z. Chen, S. Zhang, I. Levchenko, I. I. Beilis, and M. Keidar, *In vitro* demonstration of cancer inhibiting properties from stratified self-organized plasma-liquid interface, Sci. Rep. **7**, 12163 (2017).

[11] A. M. Turing, The chemical basis of morphogenesis, Bltn. Mathcal. Biology **52**, 153 (1990).

[12] T. Hwa and M. Kardar, Dissipative transport in open systems: An investigation of self-organized criticality, Phys. Rev. Lett. **62**, 1813 (1989).

[13] J. P. Trelles, Pattern formation and self-organization in plasmas interacting with surfaces, J. Phys. D **49**, 393002 (2016).

[14] W. Ning, J. Lai, J. Kruszelnicki, J. E. Foster, D. Dai, and M. J. Kushner, Propagation of positive discharges in an air bubble having an embedded water droplet, Plasma Sources Sci. Technol. **30**, 015005 (2021).

[15] P. Rumbach, A. E. Lindsay, and D. B. Go, Turing patterns on a plasma-liquid interface, Plasma Sources Sci. Technol. **28**, 105014 (2019).

[16] P. Rumbach, J. P. Clarke, and D. B. Go, Electrostatic Debye layer formed at a plasma-liquid interface, Phys. Rev. E **95**, 053203 (2017).

[17] N. Shirai, S. Uchida, F. Tochikubo, and S. Ishii, Self-organized anode pattern on surface of liquid or metal anode in atmospheric DC glow discharges, IEEE Trans. Plasma Sci. **39**, 2652 (2011).

[18] N. Shirai, S. Ibuka, and S. Ishii, Self-organization pattern in the anode spot of an atmospheric glow microdischarge using an electrolyte anode and axial miniature helium flow, Appl. Phys. Express **2**, 036001 (2009).

[19] Y. P. Raizer , *Gas Discharge Physics* (Springer, Berlin, 1991), Vol. 1.

[20] A. Armaroli, D. Eeltink, M. Brunetti, and J. Kasparian, Viscous damping of gravity-capillary waves: Dispersion relations and nonlinear corrections, Phys. Rev. Fluids **3**, 124803 (2018).

[21] K. Takamura, H. Fischer, and N. R. Morrow, Physical properties of aqueous glycerol solutions, J. Pet. Sci. Eng. **98–99**, 50 (2012).

[22] See Supplemental Material at http://link.aps.org/supplemental/10.1103/PhysRevLett.133.105301 for experimental details including example images, full data sets, and uncertainties. Theoretical details including model parameters and numerical analysis of viscous wave dispersion.

[23] A. Wilson, D. Staack, T. Farouk, A. Gutsol, A. Fridman, and B. Farouk, Self-rotating DC atmospheric-pressure discharge over a water-surface electrode: regimes of operation, Plasma Sources Sci. Technol. **17**, 045001 (2008).

[24] R. V. Raghavan, J. Qin, L. Y. Yeo, J. R. Friend, K. Takemura, S. Yokota, and K. Edamura, Electrokinetic actuation of low conductivity dielectric liquids, Sens. Actuators B **140**, 287 (2009).

[25] M. K. Tan, J. R. Friend, O. K. Matar, and L. Y. Yeo, Capillary wave motion excited by high frequency surface acoustic waves, Phys. Fluids **22**, 112112 (2010).

[26] C. L. Goodridge, W. T. Shi, H. G. E. Hentschel, and D. P. Lathrop, Viscous effects in droplet-ejecting capillary waves, Phys. Rev. E **56**, 472 (1997).

[27] J. Lai and J. E. Foster, Experimental observation of interfacial oscillations and self-organization derived from streamer-driven mechanical perturbation of a gas–liquid boundary, Plasma Sources Sci. Technol. **28**, 125003 (2019).

[28] G. J. M. Hagelaar and L. C. Pitchford, Solving the Boltzmann equation to obtain electron transport coefficients and rate coefficients for fluid models, Plasma Sources Sci. Technol. **14**, 722 (2005).

[29] V. G. Levich and C. W. Tobias, Physicochemical hydrodynamics, J. Electrochem. Soc. **110**, 251C (1963).

[30] C. F. Hayes, Water-air interface in the presence of an applied electric field, J. Phys. Chem. **79**, 1689 (1975).

[31] D. Koulova, H. Romat, and C. Louste, Experimental study of wave propagation on liquid/air surfaces under perpendicular electric field, IEEE Trans. Dielectr. Electr. Insul. **25**, 1716 (2018).

[32] S.-J. Shin, D. H. Kim, G. Bae, S. Ringe, H. Choi, H.-K. Lim, C. H. Choi, and H. Kim, On the importance of the electric double layer structure in aqueous electrocatalysis, Nat. Commun. **13**, 174 (2022).

[33] M. Sato, N. Kudo, and N. Saito, Surface tension reduction of liquid by applied electric field using vibrating jet method, IEEE Trans. Ind. Appl. **34**, 294 (1998).

[34] M. Vis, V. F. D. Peters, E. M. Blokhuis, H. N. W. Lekkerkerker, B. H. Erné, and R. H. Tromp, Effects of electric charge on the interfacial tension between coexisting aqueous mixtures of polyelectrolyte and neutral polymer, Macromolecules **48**, 7335 (2015).

[35] V. V. Yuzhakov, H.-C. Chang, and A. E. Miller, Pattern formation during electropolishing, Phys. Rev. B **56**, 12608 (1997).

[36] J. T. Stuart, Double boundary layers in oscillatory viscous flow, J. Fluid Mech. **24**, 673 (1966).

[37] L. K. Zarembo, Acoustic streaming, *in High-Intensity Ultrasonic Fields*, edited by L. D. Rozenberg (Springer, Boston, 1971), pp. 135–199, 10.1007/978-1-4757-5408-7_3.

[38] T. Srivastava, M. S. Simeni, G. Nayak, and P. J. Bruggeman, Self-organized patterns at the plasma–liquid anode interface in a helium glow discharge: Temporal development and mechanisms, Plasma Sources Sci. Technol. **31**, 085010 (2022).

[39] F. Rezaei, P. Vanraes, A. Nikiforov, R. Morent, and N. De Geyter, Applications of plasma-liquid systems: A review, Materials **12**, 2751 (2019).

[40] P. Vanraes and A. Bogaerts, The essential role of the plasma sheath in plasma–liquid interaction and its applications—A perspective, J. Appl. Phys. **129**, 220901 (2021).

[41] Q. Zhu, S. Wallentine, G.-H. Deng, J. A. Rebstock, and L. R. Baker, The solvation-induced Onsager reaction field rather than the double-layer field controls CO_2 reduction on gold, JACS Au **2**, 472 (2022).

End Matter

Appendix: New electrohydrodynamic dispersion relation—The inviscid dispersion relation is significantly affected by the strong interfacial electric field imposed on the liquid by the plasma. Namely, cations accumulate on the liquid side of the interface to form an oppositely charged layer. If interfacial charge transfer is negligible, the thickness of this polarized liquid layer is comparable to the liquid Debye layer λ or the sub-1 nm Stern layer thickness [32]. The high field between the two oppositely charged layers [41], one on the gas side and one on the liquid side, have been speculated to disrupt the hydrogen bonds in the liquid and significantly diminish the surface tension [33,34]. The high liquid conductivity and permittivity, relative to the gas phase, dictate that the plasma electric field dominates the Maxwell pressure, despite the presence of a liquid polarized layer. We hence neglect both capillary pressure and hydrostatic pressure and concentrate only on the Maxwell pressure at the interface that sustains the interfacial wave.

In the presence of an interfacial wave, this interfacial Maxwell pressure produces an in-phase component P' that sustains the wave,

$$P = \varepsilon_0 E^2/2 = \frac{\varepsilon_0}{2}(E_0 + E')^2 \sim \frac{\varepsilon E_0^2}{2} + \varepsilon_0 E_0 E' = P_0 + P', \tag{A1}$$

where ε_0 is the plasma permittivity. Yuzhakov *et al.* [35] show that the perturbation field on the interface E' due to surface curvature is

$$E' = -\frac{E_0}{2} L_p \frac{\partial^2 h}{\partial x^2}, \tag{A2}$$

where h is the surface height, and L_p is the plasma Debye length. Neglecting capillary pressure due to the intense field across the interface by the cation polarized layer in the liquid, the leading-order inviscid Euler equation of motion becomes

$$\rho \frac{\partial v}{\partial t} = -\frac{\partial P}{\partial z}. \tag{A3}$$

Combining Eqs. (A1)–(A3) and noting the kinematic condition $v = (\partial h/\partial t)$ at the liquid surface, we obtain

$$\rho \frac{\partial^2 h}{\partial t^2} = \frac{\partial}{\partial z}\left(\frac{\varepsilon E_0^2}{2} L_p \frac{\partial^2 h}{\partial x^2}\right). \tag{A4}$$

Differentiating the right hand side yields the wave equation

$$\rho \frac{\partial^2 h}{\partial t^2} = \varepsilon E_0 L_p \frac{\partial E_0}{\partial z} \frac{\partial^2 h}{\partial x^2}. \tag{A5}$$

with the wave frequency corresponding to a constant phase velocity,

$$\omega^2 = \frac{\varepsilon L_p E_0 \frac{dE_0}{dz}}{\rho} k^2. \tag{A6}$$

Neglecting the electron distribution within the plasma sheath (Debye layer), we apply the Maxwell-Poisson equation $(dE_0/dz) = qn_0$ to (A6) and yield the inviscid dispersion relation with a constant phase velocity

$$\omega_0 = \left(\frac{qn_0 L_p E_0}{\rho}\right)^{1/2} k. \tag{A7}$$